EES Solar

PAPER

View Article Online
View Journal | View Issue

Cite this: *EES Sol.*, 2025, **1**, 56

Cation optimization for bifacial surface passivation in efficient and stable perovskite solar cells†

Jie Zhao,‡[ab] Nitish Rai,‡[ab] Juan F. Benitez-Rodriguez,[c] Wenqi Yan,[ab] Luke J. Sutherland,[d] Junlin Yan,[c] Anthony S. R. Chesman,[d] Jacek Jasieniak,[ac] Jianfeng Lu[e] and Udo Bach[*ab]

Passivating the exposed surface of perovskite films is a well-established method for improving the performance of perovskite solar cells (PSCs), but the effect of similar processes on the buried interfaces remains poorly understood. Using methylammonium thiocyanate (MASCN) with a 2D perovskite passivator is known to passivate both exposed and buried surfaces through perovskite recrystallization, allowing the 2D passivator to penetrate the buried interface. However, systematic studies on the role of the thiocyanate anion (SCN^-) and different cations in this recrystallization process are lacking. Herein, we investigate thiocyanate salts with various cations – ammonium (NH_4^+), methylammonium (MA^+), ethylammonium (EA^+), and *n*-butylammonium (*n*-BA^+). Our results reveal that the SCN^- anion significantly improves the solubility of organic perovskite precursors, facilitating recrystallization regardless of the cation. The choice of cation influences the recrystallization process: MA^+, EA^+, and *n*-BA^+ lead to the formation of a horizontally oriented 2D perovskite layer that hinders charge collection, while NH_4^+ allows the 2D passivator (in our case, 4-methoxy-phenylethylammonium iodide, MEO-PEAI) to remain on the surface, enhancing device performance. Devices treated with MEO-PEAI and NH_4SCN achieved the highest open-circuit voltage and power conversion efficiency of 24.3% (V_{OC} = 1.17 V, J_{SC} = 25.1 mA cm^{-2}, FF = 82.9%). These devices also demonstrated improved stability under thermal stress at 65 °C and continuous light illumination.

Received 3rd October 2024
Accepted 9th January 2025

DOI: 10.1039/d4el00013g

rsc.li/EESSolar

Broader context

Perovskite solar cells (PSCs) represent a promising emerging technology for next-generation photovoltaics due to their high efficiency and relatively low production costs. However, further improvements in efficiency and stability are crucial to pave the way for commercialization, with defect passivation being a key area of focus. In this study, we investigate the mechanisms behind a passivation strategy that effectively targets both exposed and buried surfaces of the perovskite active layer. Building on these insights, we introduce a more effective approach through cation engineering, allowing precise control over the passivation process and mitigating the detrimental effects of surface defects. Consequently, both the efficiency and stability of the devices have been significantly improved. Our findings not only provide deeper insights into the mechanisms of defect passivation but also contribute to the development of more efficient and stable PSCs.

Introduction

State-of-the-art perovskite solar cells (PSCs) have gained significant attention over the past decade,[1–4] achieving certified power conversion efficiencies (PCEs) exceeding 26%.[5] This significant milestone is attributed to key advancements in the compositional, additive and interfacial engineering of PSCs, resulting in perovskite films with controlled crystallization and reduced defect density.[6–10] However, the detrimental effects of defects located at the interface between the perovskite films and adjacent charge transfer layers (CTLs) remain a major bottleneck for achieving higher device performance. Typically, these defects result in losses in open circuit voltage (V_{OC}) and fill factors (FF), decreasing the overall performance.[11,12]

The correlation between the V_{OC} loss and charge recombination in the bulk or at the surface of perovskite films has been extensively documented.[13–15] Typically, the solution processing of polycrystalline perovskite films *via* a conventional antisolvent method introduces significant surface defects at the interface between perovskite and CTLs.[10,15,16] Previous studies have also

[a]*ARC Center of Excellence in Exciton Science, Monash University, Victoria 3800, Australia*

[b]*Department of Chemical and Biological Engineering, Monash University, Victoria 3800, Australia. E-mail: Udo.Bach@monash.edu*

[c]*Department of Materials Science and Engineering, Monash University, Victoria 3800, Australia*

[d]*CSIRO Manufacturing, Clayton, Victoria 3168, Australia*

[e]*State Key Laboratory of Silicate Materials for Architectures, Wuhan University of Technology, Wuhan 430070, China*

† Electronic supplementary information (ESI) available. See DOI: https://doi.org/10.1039/d4el00013g

‡ These authors contributed equally to this work.

identified non-radiative recombination at the interfaces between the perovskite and CTLs as the primary cause of voltage losses for PSCs.[13,16–18] These interfaces play a critical role in facilitating charge carrier separation, transport and collection, making the high trap density at the interface inevitably result in severe non-radiative recombination and voltage losses.[11,19] Additionally, degradation of the perovskite photoabsorber due to interface defects has been shown as the principal cause for the decline in device performance.[19] Thus, effective control of these interfaces in PSCs is crucial for improving device performance.

In recent years, tremendous efforts have been dedicated to passivating the exposed upper surface of the perovskite film through various post-treatment routes, primarily because of the simplicity of the process.[10,20–23] Various passivators have been proven to be effective in enhancing the efficiency and stability of PSCs, including Lewis acid-base adducts,[24–26] wide-bandgap inorganic oxides,[27,28] and hydrophobic organic molecules.[29,30] In particular, large organic halide salts,[31–34] such as *n*-butylammonium iodide (*n*-BAI) and phenylethylammonium iodide (PEAI) have attracted considerable research interest, achieved notable success, and have been employed in many of the most efficient PSCs.[35–38] Despite the remarkable success of post-treatment passivation strategies, there is significant potential for further enhancing the performance of PSCs towards their theoretical limit through the passivation of buried interfaces.

The importance of optimizing this bottom interface is often overlooked in the perovskite community, partly because of the challenges involved in investigating the complex nanoscale buried interface.[3,39] In addition, conventional post-treatment strategies, such as employing organic halide salts, cannot be readily applied to buried interfaces due to their high solubility in perovskite precursor solvents. Recently, Liu *et al.* introduced a straightforward approach for simultaneously passivating both the upper and lower CTL interfaces using a mixture of PEAI and methylammonium thiocyanate (MASCN).[40] Passivation using this mixture, with the commonly used iso-propanol solvent (IPA), induced perovskite film recrystallization and facilitated the penetration of PEAI into the bottom interface. However, the underlying mechanism of this process and the impact of cations on recrystallization remain unclear in this previous study. Therefore, further research is essential to enhance the effectiveness of this passivation technique and improve the device performance.

Herein, we systematically explore the role of organic cations and the SCN^- anion in improving the performance of PSCs. Four thiocyanate salts were investigated: ammonium (NH_4^+), methylammonium (MA^+), ethylammonium (EA^+), and *n*-butylammonium (*n*-BA^+). It was found that the SCN^- anion notably enhances the solubility of organic perovskite precursors, such as formamidinium iodide (FAI), leading to the dissolution of the perovskite in 2-propanol and subsequent recrystallization during the post-annealing step. Consequently, irrespective of the size of the organic cation, all four thiocyanate compounds facilitate the penetration of the organic halide passivator (in this case, 4-methoxy-phenylethylammonium iodide MEO-PEAI) into the buried interface. Moreover, the cations were found to significantly influence the recrystallization of perovskite by altering the reaction product. In the case of MA^+, EA^+, and *n*-BA^+ thiocyanate salts, we observe the formation of a quasi 2D/3D perovskite heterostructure on the surface, whereas with NH_4^+ the MEO-PEAI remains on the surface and doesn't form a 2D/3D heterostructure. Remarkably, the MEO-PEAI itself served as a considerably more effective passivation agent for a 3D FAMA-based perovskite film. Consequently, PSC devices treated with MEO-PEAI and NH_4SCN demonstrate the highest V_{OC} and overall performance. The champion device achieved a PCE of 24.3% (V_{OC} = 1.17 V, J_{SC} = 25.1 mA cm^{-2}, FF = 82.9%), with enhanced stability under thermal stress (65 °C) and continuous light illumination.

Results and discussion

In this work, we investigated the impact of treating the surface of $(FAPbI_3)_{0.99}(MAPbBr_3)_{0.01}$ perovskites with MEO-PEAI, both in isolation and in conjunction with NH_4SCN, MASCN, EASCN, or BASCN salts, upon structural properties and photovoltaics performance. Fig. 1a depicts the molecular structures of these compounds. In light of recent findings that SCN^- contributes only to the recrystallization process without integrating into the perovskite crystal structure due to its thermalisation during the post-annealing step,[40] we examined the impact of altering the chain lengths of ammonium cation derivatives in thiocyanate salts on the recrystallization of perovskite films.

First, we performed scanning electron microscopy (SEM) to study the effects of thiocyanate salt post-treatment on the morphologies of both the exposed and buried surfaces of the perovskite films. To examine the buried surfaces directly, we removed the perovskite films from the substrates by peeling them off with a UV-epoxy encapsulant.[3] As depicted in Fig. 1b–e and S1,† all the samples show compact and dense buried surfaces. However, the perovskite films without any post-treatment (reference sample) displayed the smallest grain sizes and a higher density of grain boundaries, indicating relatively poor film quality. Conversely, the top surface of the reference sample (Fig. S2a†) exhibited significantly larger grains and better film quality than its buried counterpart. This difference is likely caused by the crystallization process initiating from the top perovskite–air interface during the one-step solution deposition of perovskite films *via* spin-coating. Here, the evaporation of the lower boiling point solvent (*N*,*N*-dimethylformamide, DMF) results in the formation of a solid shell that temporarily entraps the high boiling point dimethyl sulfoxide (DMSO) solvent. Although the residual DMSO is eventually eliminated with further annealing, it can lead to suboptimal crystallization and an increased density of traps at the buried interface.[41,42] Therefore, it is critical to eliminate the defects at the buried interface to enhance device performance. For the films treated with MEO-PEAI only, an improved morphology at the buried interface was observed (Fig. 2c) compared to the reference sample. Previous studies have shown that the exposed top surface undergoes reconstruction during post-treatment, triggered by the dissolution reaction process induced by IPA:[43]

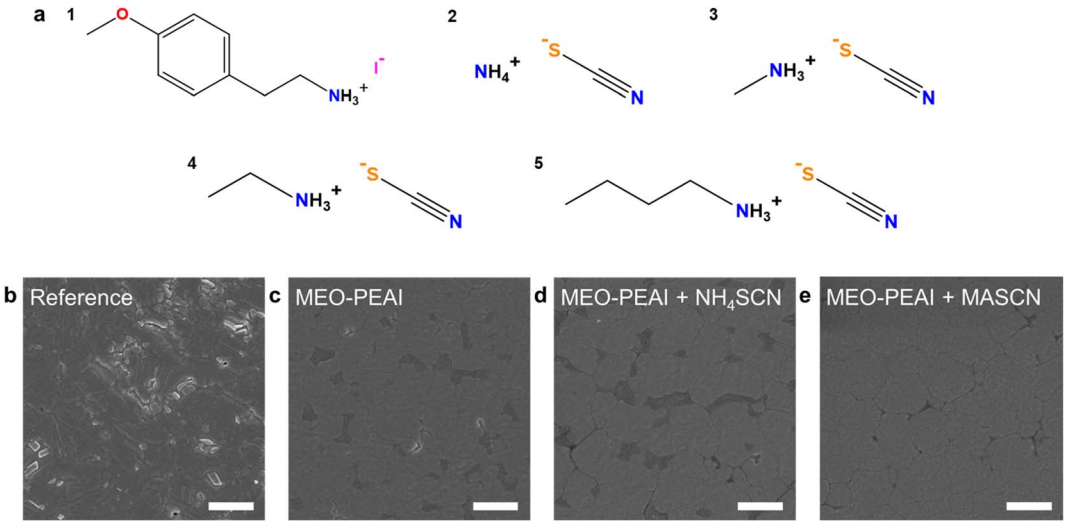

Fig. 1 (a), Molecular structures of 4-methoxy-phenylethylammonium iodide (MEO-PEAI), ammonium thiocyanate (NH_4SCN), methylammonium thiocyanate (MASCN), ethylammonium thiocyanate (EASCN) and *n*-butylammonium thiocyanate (BASCN), respectively (**1**–**5**). (b–e) Scanning electron microscopy (SEM) images of buried interface of reference, MEO-PEAI, MEO-PEAI + NH_4SCN and MEO-PEAI + MASCN treated perovskite films. Scale bars, 1 μm.

$$\mathrm{FAPbI_3} \xrightarrow{\mathrm{IPA}} \mathrm{FAI(in\ IPA)} + \mathrm{PbI_2(s)} + \mathrm{V'_{FA}} + \mathrm{V_I^{\cdot}}\left(\mathrm{V'_{FA}}: \mathrm{FA\ \ vacancy}, \mathrm{V_I^{\cdot}}: \mathrm{iodine\ \ vacancy}\right)$$

These findings suggest that during this dissolution process, IPA likely infiltrates the buried interface, primarily through the grain boundaries, leading to a recrystallization of the buried surface as well.

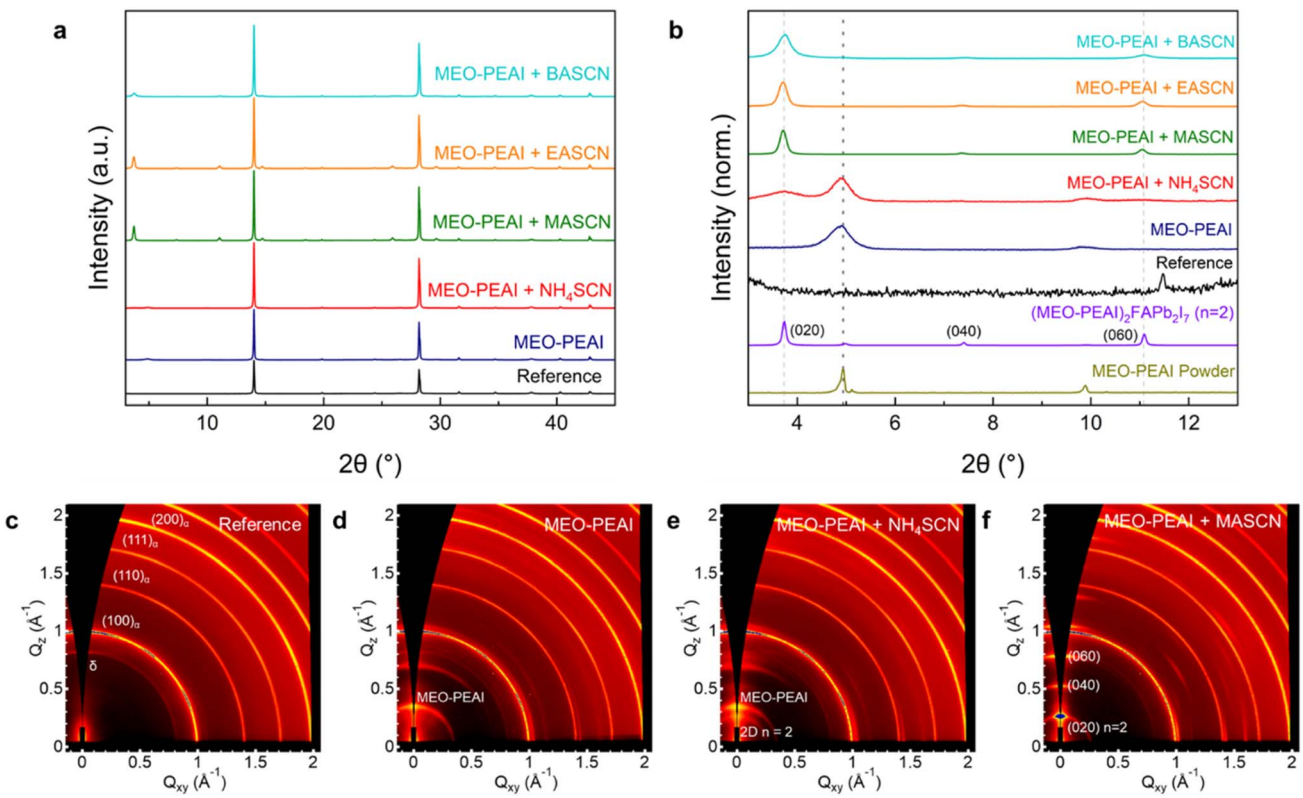

Fig. 2 (a) X-ray diffraction (XRD) patterns of perovskite films. (b) Enlarged XRD pattern in the 2θ range between 3° and 12° of perovskite films. (c–f) Two-dimensional grazing-incidence wide-angle X-ray scattering (GIWAXS) patterns of reference, MEO-PEAI, MEO-PEAI + NH_4SCN, MEO-PEAI + MASCN treated perovskite films.

A surface treatment combing MEO-PEAI and thiocyanate salts further improved the film morphology at the buried interface, as evidenced by larger grain sizes in the SEM images (Fig. 1, S1†). These improvements may be attributed to the intermediate catalytic role of the pseudohalide SCN^- during the crystallisation process, whereby its higher electronegativity relative to I^- augments its ability to form stronger ionic and hydrogen bonds with Pb^{2+} and FA^+, respectively. Nonetheless, during the post-annealing step, the limited thermal stability of SCN^- leads to its rapid volatilization and conversion into thiocyanic acid (HSCN).[44,45] This transition is crucial as it initiates the formation of a new 3D perovskite structure by effectively governing the recrystallization process, thereby promoting the growth of larger perovskite grains. As depicted in the top surface SEM images in Fig. S2,† all post-treatment solutions also significantly impact the morphologies of the films' exposed surface. While the films treated with MEO-PEAI alone and those treated with a combination of MEO-PEAI and NH_4SCN displayed similar morphologies, films treated with MASCN, EASCN, or BASCN, along with MEO-PEAI, exhibited distinct morphologies characterized by large, dark regions randomly distributed across the surface. To further investigate exposed surface morphology and roughness, atomic force microscopy (AFM) measurements were performed for the reference film, as well as samples treated with MEO-PEAI, MEO-PEAI + NH_4SCN, and MEO-PEAI + MASCN (Fig. S3†). Compared to the reference film (RMS = 27.9 nm), the samples treated with MEO-PEAI and MEO-PEAI + NH_4SCN exhibited smoother surfaces, with RMS values of 19.7 nm and 24.7 nm, respectively. However, for the MEO-PEAI + MASCN treated film, which showed large secondary dark regions in the SEM images, the surface became significantly rougher, with an RMS of 42.2 nm. Cross-sectional SEM images are presented in Fig. S4.† All films display monolithic grains extending from top to bottom, with a similar thickness of approximately 600 nm.

To further understand these morphological variations, X-ray diffraction (XRD) and two-dimensional grazing-incidence wide-angle X-ray scattering (GIWAXS) were employed. XRD patterns of both the reference and treated samples (Fig. 2a) revealed the formation of the desired perovskite phase, as evidenced by the strong reflection of (100) planes at 2θ values of 14.0°, with negligible formation of the photoinactive δ phase. Additionally, no significant peak shifts were observed for the (100) reflection after the surface treatment, implying negligible incorporation of SCN^- into the perovskite lattice. Additional peaks appeared in the low-angle region following surface treatment, as highlighted in the magnified XRD patterns (Fig. 2b). Notably, samples treated with MEO-PEAI, in isolation or in combination with NH_4SCN, exhibited a peak at $2\theta = 4.9°$, which is ascribed to the pure MEO-PEAI salt.[40] The introduction of NH_4SCN led to an additional broad peak at 3.7°. Furthermore, the addition of long-chain alkyl ammonium thiocyanate resulted in the disappearance of the 4.9° peak and enhancement of the 3.7° peak, which, when compared to the XRD pattern of the 2D perovskite $(MEO\text{-}PEAI)_2FAPb_2I_7$, suggests that MEO-PEAI was incorporated into a 2D perovskite structure ($n = 2$). These findings verify the top-view SEM (Fig. S2†) results, showing that MEO-PEAI and MEO-PEAI + NH_4SCN samples exhibited similar surface morphologies, with MEO-PEAI remaining on the surface. In contrast, for MASCN, EASCN, and BASCN samples, a 2D perovskite film formation was observed on the surface. Furthermore, the darker features observed in the SEM images typically arise from the regions of lower average atomic number. Given that 2D perovskite possesses a lower lead density compared to 3D perovskite, the large, randomly distributed darker regions in the SEM images likely originate from 2D perovskites.[46]

GIWAXS measurements (Fig. 2c–f and S5†) were performed to study the orientation of the crystallite domains in the films. Both the reference and modified samples exhibited a similar orientation of the predominant (100) facets in out-of-plane directions. The GIWAXS patterns for MEO-PEAI and MEO-PEAI + NH_4SCN were consistent with the XRD results, confirming the presence of crystalline MEO-PEAI and indicating that a small portion of the MEO-PEAI in the MEO-PEAI + NH_4SCN samples was incorporated into a 2D perovskite phase. For MASCN, EASCN, and BASCN samples, the complete conversion of MEO-PEAI into 2D perovskite was observed. Interestingly, the 2D perovskite demonstrated a stronger preference for horizontal orientation as the alkyl chain length increased. We speculate that this is due to the slower evaporation rate of SCN^- attributed to the longer alkyl chains, resulting in a reduced crystallization rate of 2D perovskite and, consequently, a more horizontally oriented 2D perovskite structure at the surface.

To explore the influence of SCN^- on the perovskite conversion process, we investigated the solubility of the dominant organic halide perovskite precursor, FAI, in IPA, either with or without the thiocyanate salts. As illustrated in Fig. S6a,† the solubility of FAI in IPA was found to significantly increase upon the addition of the various thiocyanate salts. To isolate the impact of the cation we conducted solubility tests for FAI with various ammonium salts – MEO-PEAI, NH_4Cl and NH_4SCN (Fig. S6b†). We observed that neither MEO-PEAI nor ammonium chloride notably improves the solubility of FAI in IPA, proving SCN^- ion is critical for improving solubility. Furthermore, we observed direct evidence of the dissolution of perovskite being assisted by the presence of SCN^- by conducting solubility tests of pre-synthesized $FAPbI_3$ in IPA (Fig. S6c†). Initially, $FAPbI_3$ exhibited minimal solubility in IPA, retaining its black appearance within the solvent. However, upon the introduction of SCN^-, a significant portion of the black powder transitioned to yellow, indicative of the conversion to PbI_2, stemming from the dissolution of FAI and the subsequent breakdown of the perovskite's 3D structure. We then conducted XPS measurements on peeled-off perovskite thin films to directly investigate the presence of MEO-PEAI at the buried interfaces, using oxygen as the identifying element. As shown in Fig. S7,† the reference film and the film treated with MEO-PEAI exhibit only a weak oxygen peak, likely caused by contaminants. In contrast, the samples treated with SCN^- show a much more pronounced oxygen peak, confirming the presence of MEO-PEAI.

Based on these observations, we propose the following mechanism underlying the formation of 2D perovskite and the grain recrystallization process upon SCN^- treatment. Firstly, the introduction of SCN^- results in the dissolution of FA^+ in IPA, facilitating the grain regrowth process. Next, the increased availability of FA^+, along with MEO-PEA^+ in IPA, promotes the reaction with exposed PbI_2, leading to the formation of 2D ($n = 2$) perovskite. Notably, the behavior of NH_4SCN differed from other thiocyanate salts. To understand this discrepancy, we conducted Fourier transform infrared spectroscopy (FTIR) measurements (Fig. S8†) on surface treated perovskite films that were yet to be annealed to assess the potential peak shifts attributable to the SCN^- ion. For samples treated with MASCN, EASCN, and BASCN, we observed a blue shift in the C≡N stretching vibration, indicating stronger interactions between SCN^- and perovskite. This is likely due to the interaction with FA^+, which, unlike MA^+, EA^+, and BA^+, offers a greater affinity for bonding with SCN^-. This is facilitated by reduced steric hindrance and the enhanced hydrogen-bonding capabilities provided by its two NH_2 groups. The resulting complex appears to promote both the dissolution and recrystallization processes within the perovskite structure. Conversely, the C≡N bond stretching vibration remained unchanged in the presence of NH_4SCN, suggesting a predominantly electrostatic interaction between NH_4^+ and SCN^-. This observation can be attributed to the minimal steric effects and the proximity allowed by the small size of NH_4^+, facilitating a strong ionic interaction.

To investigate the effects of post-treatment on the carrier dynamics and photoluminescence (PL) properties of the perovskite films, we performed both steady-state photoluminescence and time-resolved photoluminescence (TRPL) measurements. These experiments were performed on a perovskite/glass architecture to evaluate PL emissions and carrier dynamics at both the exposed surface and the buried interface, using a 420 nm laser. This wavelength primarily excites the illuminated surface, with a penetration depth of approximately 100 nm.[47,48] Firstly, the PL spectra were recorded to examine the emission associated with the 2D perovskite peak and the 3D perovskite peak intensity. As shown in Fig. S9a and c,† MEO-PEAI effectively suppresses non-radiative recombination near the exposed surface, leading to enhanced PL intensity for the 3D perovskite peak. Samples treated with MASCN exhibit a prominent 2D perovskite peak at approximately 585 nm, whereas NH_4SCN treated samples show only a weak 2D PL signal, indicating the formation of a limited amount of 2D perovskite, consistent with the XRD results. Conversely, Fig. S9b and d† reveal that samples treated with SCN^- exhibit enhanced PL intensity without any detectable 2D perovskite peak. Together with XPS data (Fig. S7†), these results support the hypothesis that SCN^- facilitates perovskite recrystallization, enabling the

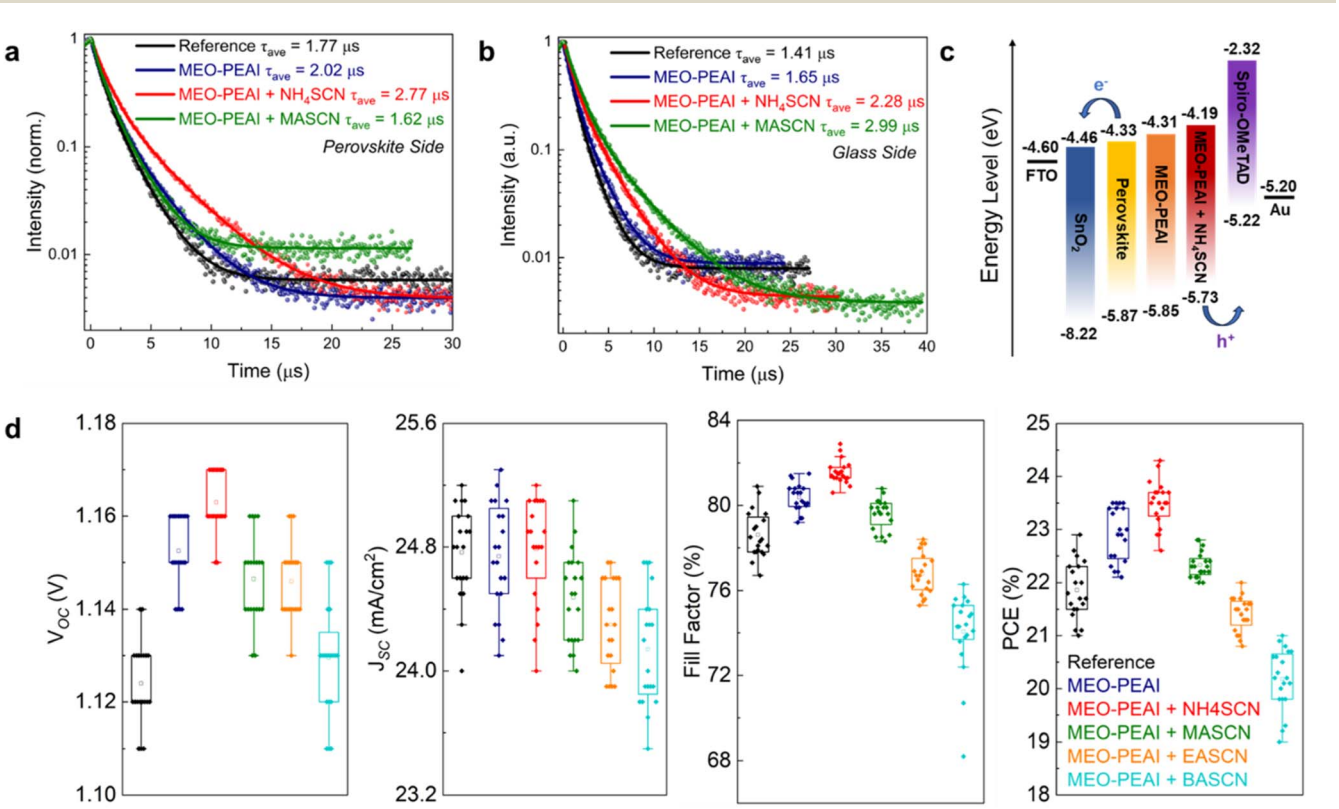

Fig. 3 (a and b) Time-resolved photoluminescence (TRPL) spectra of reference, MEO-PEAI, MEO-PEAI + NH_4SCN, MEO-PEAI + MASCN treated perovskite films excited from (a) the perovskite side and (b) the glass side. (c) Schematic representation of energy band diagram of PSCs. (d) Statistic photovoltaic parameters (reverse scan) of a batch of PSCs: open-circuit voltage (V_{OC}), short-circuit current density (J_{SC}), fill factor (FF), and PCE.

penetration of MEO-PEAI into the buried interface, where it effectively passivates defects.

Fig. 3a and S10a† show the PL decay curves for samples excited from the perovskite side. As depicted in Table S1,† the average carrier lifetime recorded for the reference film was 1.77 μs, with an increase to 2.02 μs and 2.77 μs for MEO-PEAI and MEO-PEAI + NH_4SCN samples, respectively, suggesting that MEO-PEAI effectively passivates surface defects, thereby minimizing nonradiative recombination pathways. Conversely, the introduction of 2D/3D heterostructures (MASCN, EASCN, and BASCN treatments) resulted in a decrease in carrier lifetimes, implying that the presence of parallel-oriented 2D perovskite layers restricts the carrier mobility, likely due to the presence of relatively long chain organic barriers.[17] TRPL measurements recorded by exciting the buried perovskite interface from the glass side (Fig. 3b and S10b†) further reveal that the combination of MEO-PEAI and SCN^- significantly enhances the carrier lifetime, indicating effective passivation of the bulk and/or buried surface. This observation aligns with the PL results. Notably, among the four tested SCN^- salts, only NH_4SCN was capable of enhancing lifetimes at both the exposed surface and the buried interface simultaneously.

To study the effect of post-treatment on interface energy band alignment, ultraviolet photoelectron spectroscopy (UPS) measurements were performed. As shown in Fig. 3c, the valence band minimum values (VBM) of the reference, MEO-PEAI and MEO-PEAI + NH_4SCN samples are −5.87, −5.85 and −5.73 eV, respectively (Fig. S11†), while the samples modified with MASCN, EASCN and BASCN exhibited deeper VBM levels than NH_4SCN (Table S2†). The conduction band minimum (CBM) was approximated by subtracting the optical bandgap from the VBM, which is derived from the Tauc plot (Fig. S12†). Post-treatment with MEO-PEAI + NH_4SCN resulted in the smallest energy level offset (ΔE) of 0.51 eV for hole transfer between the highest occupied molecular orbital (HOMO) of the hole transport material (HTM) spiro-OMeTAD ($E_{HOMO} \sim -5.22$ eV)[49] and the perovskite, indicating a reduced theoretical voltage loss.

We subsequently fabricated solar cells to study the impact of post-treatment on photovoltaic performance. We used a conventional n–i–p structure, employing SnO_2 and spiro-OMeTAD as the electron transport layer (ETL) and hole transport layer (HTL), respectively. Fig. 3d summarizes the photovoltaic performance parameters of a batch of PSCs subjected to various post-treatment solutions. To ensure statistical significance, 20 devices were fabricated for each group. It was observed that the V_{OC} improved from an average of ∼1.12 to ∼1.15 V after treatment with MEO-PEAI. This enhancement in V_{OC} was further increased by 10 mV to an average of 1.16 V following the addition of NH_4SCN. Conversely, the application of MASCN, EASCN, and BASCN led to a decrease in V_{OC}, likely due to the increased non-radiative recombination as evidenced by the reduction in carrier lifetime. The J_{SC} remained relatively consistent across the reference, MEO-PEAI and MEO-PEAI + NH_4SCN samples. However, in samples treated with MASCN, BASCN, and EASCN, the J_{SC} decreased gradually due to the formation of more horizontally oriented 2D perovskite on top, which hindered efficient charge transport. The FF demonstrated a similar trend as the V_{OC}. Consequently, samples treated with MEO-PEAI and NH_4SCN exhibited the highest average PCE, having a mean value of ∼23.5%.

Fig. 4 illustrates the detailed device characterisation of the champion devices. Given the negative impact of MASCN, EASCN and BASCN on the PCE, we did not conduct further studies on these devices. To enhance the J_{SC}, an anti-reflective layer of 100 nm lithium fluoride (LiF) was evaporated on the glass side of the substrate (Fig. S13†). As demonstrated in Fig. 4a, the champion device treated with MEO-PEAI + NH_4SCN achieved a PCE of 24.3%, with a V_{OC} of 1.17 V, a J_{SC} of 25.1 mA cm^{-2} and a FF of 82.9% in the reverse scan. For comparison, the champion PCE for the reference device and MEO-PEAI device are 22.9% and 23.5%, respectively. The *J–V* curves in both scan directions and detailed photovoltaic parameters are shown in Fig. S14.† As discussed above, the increase in PCE of devices treated with MEO-PEAI + NH_4SCN is primarily attributed to the enhanced V_{OC} and FF, which can be linked to their improved film morphology and suppressed non-radiative recombination. To avoid overestimating the PCE due to hysteresis, we also measured the stabilised power output (SPO) for the devices (Fig. 4b). The SPO of the reference, MEO-PEAI and MEO-PEAI + NH_4SCN devices were 22.7%, 23.2% and 23.8%, respectively. Fig. 4c shows the incident photon-to-current conversion efficiency (IPCE) spectra of these devices. All three devices exhibited similar IPCE profiles, with an integrated J_{SC} of 24.5 mA cm^{-2}, which is consistent with the results from *J–V* curves.

Additionally, trap densities in perovskite films were evaluated using the space-charge-limited current (SCLC) method, based on *J–V* measurement of electron-only devices under dark conditions (Fig. S15†). The results revealed that perovskite films treated with MEO-PEAI or MEO-PEAI + NH_4SCN exhibited lower defect densities compared to the reference film. Specifically, the defect densities in the reference film and the MEO-PEAI + NH_4SCN treated film were 4.44×10^{15} cm^{-3} and 1.8×10^{15} cm^{-3}, respectively. These findings highlight the effectiveness of MEO-PEAI + NH_4SCN passivation in reducing trap density and improving film quality.

To gain deeper insights into the improvement in V_{OC} and FF, ideality factor (n) was derived from the relationship between V_{OC} and light intensity. As shown in Fig. S16,† V_{OC} was plotted as a function of the logarithm of light intensity and fitted using the equation: $V_{OC} = n\frac{kT}{q}\ln(I)$, where n is the ideality factor, k is the Boltzmann constant, T is absolute temperature, q is the elementary charge, and I is the illumination intensity. A smaller ideality factor, closer to 1, indicates more effective suppression of non-radiative recombination.[50] Compared to the reference device ($n = 1.49$), devices treated with MEO-PEAI and MEO-PEAI + NH_4SCN exhibited reduced ideality factors of 1.44 and 1.39, respectively. We further calculated dark ideality factors from dark *J–V* characteristics (Fig. S17†). Using the equation: $n_d = \frac{q}{kT}J(V)\left(\frac{dJ}{dV}\right)^{-1}$,[51] the dark ideality factor for the MEO-PEAI + NH_4SCN treated device was found to be $n_d = 1.39$, significantly lower than that of the reference device (n_d =1.57). These results, consistent with the light-intensity-based

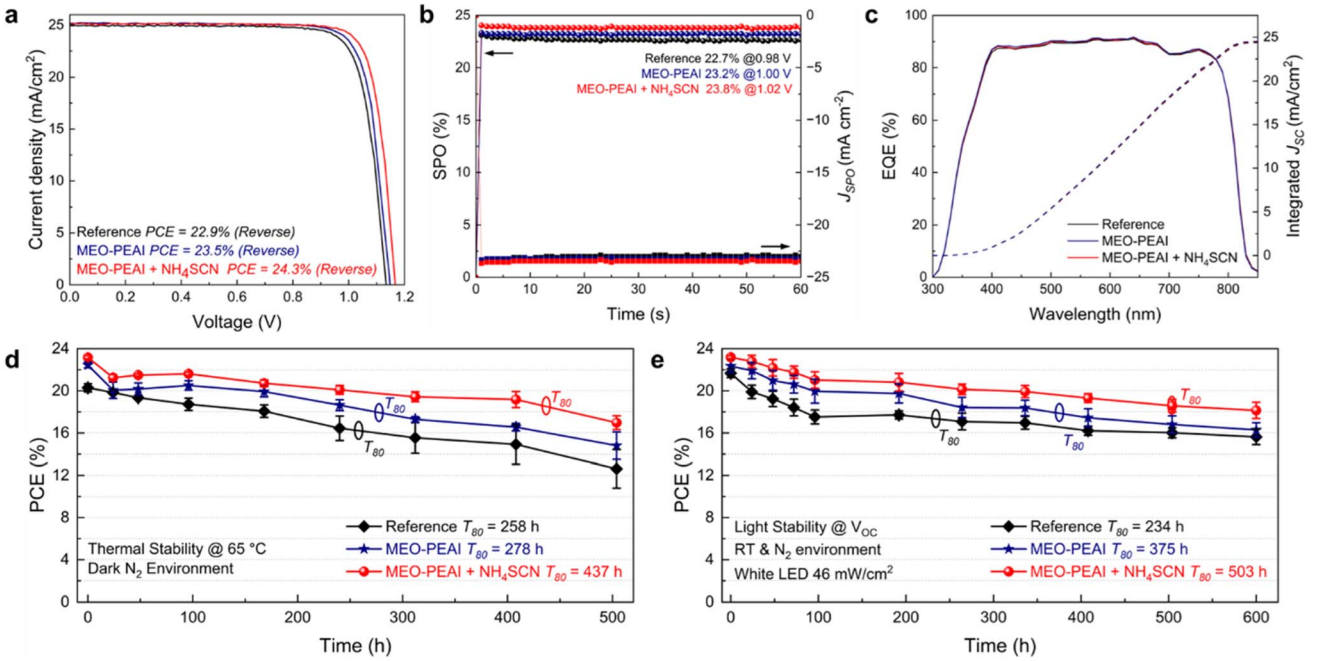

Fig. 4 $(FAPbI_3)_{0.99}(MAPbBr_3)_{0.01}$ perovskite solar cell characterization. (a), *J*–*V* characteristics of the champion devices (mask area: 0.09 cm^2). (b) Stabilized power output of the champion devices. (c) External quantum efficiency (EQE) and integrated J_{SC} of the champion devices. (d) Thermal stability of unencapsulated PSCs tested at 65 °C in a dark N_2 environment. (e) Light stability of unencapsulated PSCs test under a continuous white LED light (46 mW cm^{-2} average irradiance) at V_{OC} in a N_2 environment at room temperature.

measurements, confirm the effectiveness of MEO-PEAI + NH_4SCN in suppressing non-radiative recombination, leading to improved V_{OC} and FF.

Finally, we compared the stability of the devices under thermal stress and continuous illumination. Fig. 4d demonstrates the thermal stability of unencapsulated PSCs at 65 °C in a dark nitrogen environment. It was found that the devices treated with MEO-PEAI and MEO-PEAI + NH_4SCN exhibited a sharp initial decrease in the first 24 hours, followed by a slower decrease. The PCE of the MEO-PEAI and MEO-PEAI + NH_4SCN treated devices ultimately decreased to 80% of the initial value after 278 hours and 437 hours, respectively. In contrast, although the reference samples showed a relatively constant degradation rate, they degraded to the same extent more quickly, reaching 80% of the initial PCE after 258 hours. Next, we tested the light stability of the devices under continuous white LED (46 mW cm^{-2}) illumination at open circuit conditions in a nitrogen environment at room temperature. As depicted in Fig. 4e, the MEO-PEAI + NH_4SCN devices demonstrated superior stability, maintaining 80% of their initial PCE after 503 hours, while the reference and MEO-PEAI devices decreased to 80% of the initial PCE after just 234 hours and 375 hours, respectively. The enhanced stability of the MEO-PEAI + NH_4SCN treated devices can be attributed to the significant improvements in film quality achieved through this treatment. The combination of MEO-PEAI and NH_4SCN simultaneously passivates both the exposed and buried interfaces, reducing trap densities and suppressing non-radiative recombination. These enhancements collectively mitigate key degradation pathways, such as ion migration and trap-assisted recombination, which are well-known contributors to efficiency losses under thermal and light stress.[52,53]

Conclusion

In conclusion, we demonstrated that the performance of PSCs can be improved by treating the perovskite film surface with MEO-PEAI in conjunction with thiocyanate salts. Morphological and structural studies revealed the critical role of SCN^- ions and alkylammonium cations on the dynamic recrystallization of the perovskite film and the 2D formation processes, leading to bifacial surface passivation. The dissolution of perovskite catalysed by thiocyanate salts in IPA was identified as the driving factor for facilitating the recrystallization process at both interfaces, thereby improving the film morphology and subsequent PSC performance. Notably, the combined use of MEO-PEAI and NH_4SCN post treatment resulted in a power conversion efficiency of up to 24.3%, along with a superior thermal and light stability. While the present study investigated PSCs adopting a n–i–p device architecture, it is expected that this technique can be also be used for inverted PSCs and may demonstrate further improvements in the stability. Future studies will benefit from the strategy presented herein to develop efficient and stable PSCs for commercialization.

Experimental methods

Materials

Unless otherwise specified, all materials were purchased from either Alfa Aesar or Sigma-Aldrich. FAI, MAI, MABr, MACl, MEO-

PEAI, MASCN, EASCN and BASCN were purchased from Greatcell Solar Ltd. Spiro-OMeTAD and FK209 Co(III) TFSI Salt were purchased from Luminescence Technology Corp.

Preparation of precursor solutions

The perovskite precursor solutions were prepared in a N_2 glovebox. For the $FAPbI_3$ solution (1.4 M), 476.1 mg PbI_2, 162.5 mg FAI and 22.8 mg MACl were mixed in a 675 μL mixture of anhydrous *N*,*N*-dimethylformamide (DMF) and anhydrous dimethyl sulfoxide (DMSO) (v : v = 8 : 1). For the $MAPbBr_3$ solution, 101.1 mg $PbBr_2$, 30.8 mg MABr and 6.1 mg MACl were mixed in 180 μL of mixture of DMF and DMSO (v : v = 8 : 1). Subsequently, 1% (v/v) of the $MAPbBr_3$ solution was introduced into the $FAPbI_3$ solution to make the $(FAPbI_3)_{0.99}(MAPbBr_3)_{0.01}$ precursor solution. For post-treatment solutions, 16 mM of MEO-PEAI and 10 mM of the respective thiocyanate salt were added to 2-propanol.

A spiro-OMeTAD solution was prepared by dissolving 73 mg spiro-OMeTAD in 1 mL chlorobenzene. Then 30 μL 4-*tert*-butylpyridine, 18 μL LiTFSI (520 mg mL^{-1} in acetonitrile) and 9 μL FK209 (300 mg mL^{-1} in acetonitrile) were added, followed by stirring in a glove box for over 2 hours.

Device fabrication

FTO-coated glass substrates were ultrasonically cleaned serval times with detergent, deionized water and ethanol for 15 min each. After drying under a stream of nitrogen, substrates were treated with UV plasma for 15 min before use. The SnO_2 ETL was deposited by a chemical bath deposition method (CBD) following a previous report.[54] The substrates were then treated by UV plasma for 15 min again prior to the deposition of perovskite. The perovskite precursor solutions were spin coated at 1000 rpm for 10 s, followed by a subsequent spin-coating step at 5000 rpm for 30 s (both at a 2000 rpm s^{-1} ramp). Ten seconds into the 5000 rpm setting, 120 μL of ethyl acetate was deposited onto the center of the substrate. Subsequently, the film was annealed at 100 °C for 60 min. Following this, the post-treatment solution was applied to the perovskite film for 5 seconds, followed by spin coating at 5000 rpm for 30 seconds, and then annealed at 100 °C for an additional 5 min. The spiro-OMeTAD solution was spin coated at 3000 rpm for 30 seconds as the hole transport material (HTM). Finally, an 80 nm gold layer was deposited by thermal evaporation.

Material characterization

SEM images were captured using an FEI Nova NanoSEM 450 FEG scanning electron microscope with a beam voltage of 5 kV.

XRD data were collected with a Bruker D8 Advance diffractometer (Cu-Kα (λ = 0.15406 nm) radiation).

UV-visible transmission and reflection spectra were measured using a PerkinElmer Lambda 1050 spectrometer fitted with an integrating sphere. Absorption spectra were calculated from the transmission and reflection spectra (Absorptance = 100% − Transmission (%) − Reflection (%)). PL and TRPL was measured by a PicoQuant FT300 system. The excitation was generated by a 422 nm pulse laser, with the laser intensity kept constant for all sample measurements.

XPS and UPS results were collected using a Thermo Nexsa Surface Analysis system. The excitation sources are monochromatic Al-Kα.

FTIR spectra were collected by using PerkinElmer Spectrum Two equipped with diamond/ZnSe ATR.

GIWAXS measurements were performed at the SAXS/WAXS beamline at the Australian Synchrotron. The beam energy was fixed at 15 keV. The scattering patterns were collected using an in-vacuum Dectris Pilatus 2 M detector with a total exposure time of 3 s. An incident angle of 0.4° which is higher than the critical angle was used to probe the entire depth of the perovskite film. The sample-to-detector distance was calibrated to be ~66 cm using a silver behenate standard.

Device characterization

J–V characteristics were collected using a BioLogic VMP3 potentiostat source meter under 1-sun illumination (100 mW cm^{-2}) (An Oreil solar simulator equipped with a xenon lamp and an AM 1.5G filter). The solar intensity was calibrated using a Si-reference (KG3 filter) calibrated by Enli Tech. Optoelectronic Calibration lab. The *J–V* curves were measured in both forward and reverse scan direction between −0.1 to 1.2 V with a voltage step of 10 mV and a scan rate of 50 mV s^{-1}. All devices were tested using a black metal mask with an aperture area of 0.09 cm^2. External quantum efficiency (EQE) measurements were performed using an incident photon-to-current conversion efficiency (IPCE) apparatus from Peccell Technologies, Inc (PEC-S20), without background illumination.

Data availability

The data supporting this article have been included in the main text and the ESI.†

Conflicts of interest

The authors declare no competing interests.

Acknowledgements

This work was financially supported by the Australian Research Council through the Centre of Excellence in Exciton Science (CE170100026) and additional grants (DP160104575 and LE170100235). The authors acknowledge financial support from the Australian Government through the Australian Renewable Energy Agency (ARENA) and the Australian Centre for Advanced Photovoltaics (ACAP). The authors acknowledge the National Natural Science Foundation of China (52472248). A portion of this research was undertaken on Small/Wide Angle X-Ray Scattering Beamline at the Australian Synchrotron, part of ANSTO. The authors acknowledge the use of facilities within the Monash Centre for Electron Microscopy (MCEM), Monash X-Ray Platform (MXP).

References

1 R. Azmi, E. Ugur, A. Seitkhan, F. Aljamaan, A. S. Subbiah, J. Liu, G. T. Harrison, M. I. Nugraha, M. K. Eswaran, M. Babics, Y. Chen, F. Xu, T. G. Allen, A. u. Rehman, C.-L. Wang, T. D. Anthopoulos, U. Schwingenschlögl, M. De Bastiani, E. Aydin and S. De Wolf, *Science*, 2022, **376**, 73–77.

2 J. Jeong, M. Kim, J. Seo, H. Lu, P. Ahlawat, A. Mishra, Y. Yang, M. A. Hope, F. T. Eickemeyer, M. Kim, Y. J. Yoon, I. W. Choi, B. P. Darwich, S. J. Choi, Y. Jo, J. H. Lee, B. Walker, S. M. Zakeeruddin, L. Emsley, U. Rothlisberger, A. Hagfeldt, D. S. Kim, M. Grätzel and J. Y. Kim, *Nature*, 2021, **592**, 381–385.

3 C. Luo, G. Zheng, F. Gao, X. Wang, C. Zhan, X. Gao and Q. Zhao, *Nat. Photonics*, 2023, **17**, 856–864.

4 Y. Yang, C. Liu, Y. Ding, B. Ding, J. Xu, A. Liu, J. Yu, L. Grater, H. Zhu, S. S. Hadke, V. K. Sangwan, A. S. R. Bati, X. Hu, J. Li, S. M. Park, M. C. Hersam, B. Chen, M. K. Nazeeruddin, M. G. Kanatzidis and E. H. Sargent, *Nat. Energy*, 2024, **9**, 316–323.

5 *Best research-cell efficiency chart*, 2024, **www.nrel.gov/pv/cell-efficiency.html**.

6 N. J. Jeon, J. H. Noh, W. S. Yang, Y. C. Kim, S. Ryu, J. Seo and S. I. Seok, *Nature*, 2015, **517**, 476–480.

7 D. Bi, C. Yi, J. Luo, J.-D. Décoppet, F. Zhang, S. M. Zakeeruddin, X. Li, A. Hagfeldt and M. Grätzel, *Nat. Energy*, 2016, **1**, 16142.

8 S.-H. Turren-Cruz, A. Hagfeldt and M. Saliba, *Science*, 2018, **362**, 449–453.

9 M. Xiao, F. Huang, W. Huang, Y. Dkhissi, Y. Zhu, J. Etheridge, A. Gray-Weale, U. Bach, Y.-B. Cheng and L. Spiccia, *Angew. Chem., Int. Ed.*, 2014, **53**, 9898–9903.

10 Q. Jiang, Y. Zhao, X. Zhang, X. Yang, Y. Chen, Z. Chu, Q. Ye, X. Li, Z. Yin and J. You, *Nat. Photonics*, 2019, **13**, 460–466.

11 Y. Wang, M. Han, R. Wang, J. Zhao, J. Zhang, H. Ren, G. Hou, Y. Ding, Y. Zhao and X. Zhang, *J. Mater. Chem. A*, 2023, **11**, 8573–8598.

12 N.-G. Park and H. Segawa, *ACS Photonics*, 2018, **5**, 2970–2977.

13 A. Buin, P. Pietsch, J. Xu, O. Voznyy, A. H. Ip, R. Comin and E. H. Sargent, *Nano Lett.*, 2014, **14**, 6281–6286.

14 J. S. Manser, M. I. Saidaminov, J. A. Christians, O. M. Bakr and P. V. Kamat, *Acc. Chem. Res.*, 2016, **49**, 330–338.

15 G.-J. A. H. Wetzelaer, M. Scheepers, A. M. Sempere, C. Momblona, J. Ávila and H. J. Bolink, *Adv. Mater.*, 2015, **27**, 1837–1841.

16 G. Wu, R. Liang, M. Ge, G. Sun, Y. Zhang and G. Xing, *Adv. Mater.*, 2022, **34**, 2105635.

17 G. Yang, Z. Ren, K. Liu, M. Qin, W. Deng, H. Zhang, H. Wang, J. Liang, F. Ye, Q. Liang, H. Yin, Y. Chen, Y. Zhuang, S. Li, B. Gao, J. Wang, T. Shi, X. Wang, X. Lu, H. Wu, J. Hou, D. Lei, S. K. So, Y. Yang, G. Fang and G. Li, *Nat. Photonics*, 2021, **15**, 681–689.

18 D. Luo, W. Yang, Z. Wang, A. Sadhanala, Q. Hu, R. Su, R. Shivanna, G. F. Trindade, J. F. Watts, Z. Xu, T. Liu, K. Chen, F. Ye, P. Wu, L. Zhao, J. Wu, Y. Tu, Y. Zhang, X. Yang, W. Zhang, R. H. Friend, Q. Gong, H. J. Snaith and R. Zhu, *Science*, 2018, **360**, 1442–1446.

19 N. K. Noel, S. N. Habisreutinger, B. Wenger, Y.-H. Lin, F. Zhang, J. B. Patel, A. Kahn, M. B. Johnston and H. J. Snaith, *Adv. Energy Mater.*, 2020, **10**, 1903231.

20 S. Sidhik, Y. Wang, M. De Siena, R. Asadpour, A. J. Torma, T. Terlier, K. Ho, W. Li, A. B. Puthirath, X. Shuai, A. Agrawal, B. Traore, M. Jones, R. Giridharagopal, P. M. Ajayan, J. Strzalka, D. S. Ginger, C. Katan, M. A. Alam, J. Even, M. G. Kanatzidis and A. D. Mohite, *Science*, 2022, **377**, 1425–1430.

21 A. A. Sutanto, P. Caprioglio, N. Drigo, Y. J. Hofstetter, I. Garcia-Benito, V. I. E. Queloz, D. Neher, M. K. Nazeeruddin, M. Stolterfoht, Y. Vaynzof and G. Grancini, *Chem*, 2021, **7**, 1903–1916.

22 Q. Jiang, J. Tong, Y. Xian, R. A. Kerner, S. P. Dunfield, C. Xiao, R. A. Scheidt, D. Kuciauskas, X. Wang, M. P. Hautzinger, R. Tirawat, M. C. Beard, D. P. Fenning, J. J. Berry, B. W. Larson, Y. Yan and K. Zhu, *Nature*, 2022, **611**, 278–283.

23 C. Luo, Y. Zhao, X. Wang, F. Gao and Q. Zhao, *Adv. Mater.*, 2021, **33**, 2103231.

24 Y. Shao, Z. Xiao, C. Bi, Y. Yuan and J. Huang, *Nat. Commun.*, 2014, **5**, 5784.

25 Y. Lin, B. Chen, F. Zhao, X. Zheng, Y. Deng, Y. Shao, Y. Fang, Y. Bai, C. Wang and J. Huang, *Adv. Mater.*, 2017, **29**, 1700607.

26 N. K. Noel, A. Abate, S. D. Stranks, E. S. Parrott, V. M. Burlakov, A. Goriely and H. J. Snaith, *ACS Nano*, 2014, **8**, 9815–9821.

27 S. Yang, S. Chen, E. Mosconi, Y. Fang, X. Xiao, C. Wang, Y. Zhou, Z. Yu, J. Zhao, Y. Gao, F. De Angelis and J. Huang, *Science*, 2019, **365**, 473–478.

28 Y. Bai, Y. Lin, L. Ren, X. Shi, E. Strounina, Y. Deng, Q. Wang, Y. Fang, X. Zheng, Y. Lin, Z.-G. Chen, Y. Du, L. Wang and J. Huang, *ACS Energy Lett.*, 2019, **4**, 1231–1240.

29 Y. Liu, S. Akin, L. Pan, R. Uchida, N. Arora, J. V. Milić, A. Hinderhofer, F. Schreiber, A. R. Uhl, S. M. Zakeeruddin, A. Hagfeldt, M. I. Dar and M. Grätzel, *Sci. Adv.*, 2019, **5**, eaaw2543.

30 B. Li, Y. Zhang, L. Fu, T. Yu, S. Zhou, L. Zhang and L. Yin, *Nat. Commun.*, 2018, **9**, 1076.

31 Y. Cho, A. M. Soufiani, J. S. Yun, J. Kim, D. S. Lee, J. Seidel, X. Deng, M. A. Green, S. Huang and A. W. Y. Ho-Baillie, *Adv. Energy Mater.*, 2018, **8**, 1703392.

32 S. Gharibzadeh, B. Abdollahi Nejand, M. Jakoby, T. Abzieher, D. Hauschild, S. Moghadamzadeh, J. A. Schwenzer, P. Brenner, R. Schmager, A. A. Haghighirad, L. Weinhardt, U. Lemmer, B. S. Richards, I. A. Howard and U. W. Paetzold, *Adv. Energy Mater.*, 2019, **9**, 1803699.

33 T. M. Koh, V. Shanmugam, X. Guo, S. S. Lim, O. Filonik, E. M. Herzig, P. Müller-Buschbaum, V. Swamy, S. T. Chien, S. G. Mhaisalkar and N. Mathews, *J. Mater. Chem. A*, 2018, **6**, 2122–2128.

34 Y. Lin, Y. Bai, Y. Fang, Z. Chen, S. Yang, X. Zheng, S. Tang, Y. Liu, J. Zhao and J. Huang, *J. Phys. Chem. Lett.*, 2018, **9**, 654–658.

35 H. Min, D. Y. Lee, J. Kim, G. Kim, K. S. Lee, J. Kim, M. J. Paik, Y. K. Kim, K. S. Kim, M. G. Kim, T. J. Shin and S. Il Seok, *Nature*, 2021, **598**, 444–450.
36 M. Kim, J. Jeong, H. Lu, T. K. Lee, F. T. Eickemeyer, Y. Liu, I. W. Choi, S. J. Choi, Y. Jo, H.-B. Kim, S.-I. Mo, Y.-K. Kim, H. Lee, N. G. An, S. Cho, W. R. Tress, S. M. Zakeeruddin, A. Hagfeldt, J. Y. Kim, M. Grätzel and D. S. Kim, *Science*, 2022, **375**, 302–306.
37 J. Park, J. Kim, H.-S. Yun, M. J. Paik, E. Noh, H. J. Mun, M. G. Kim, T. J. Shin and S. I. Seok, *Nature*, 2023, **616**, 724–730.
38 Q. Tan, Z. Li, G. Luo, X. Zhang, B. Che, G. Chen, H. Gao, D. He, G. Ma, J. Wang, J. Xiu, H. Yi, T. Chen and Z. He, *Nature*, 2023, **620**, 545–551.
39 X. Yang, D. Luo, Y. Xiang, L. Zhao, M. Anaya, Y. Shen, J. Wu, W. Yang, Y.-H. Chiang, Y. Tu, R. Su, Q. Hu, H. Yu, G. Shao, W. Huang, T. P. Russell, Q. Gong, S. D. Stranks, W. Zhang and R. Zhu, *Adv. Mater.*, 2021, **33**, 2006435.
40 Z. Liu, C. Zhu, H. Luo, W. Kong, X. Luo, J. Wu, C. Ding, Y. Chen, Y. Wang, J. Wen, Y. Gao and H. Tan, *Adv. Energy Mater.*, 2023, **13**, 2203230.
41 S. Chen, X. Dai, S. Xu, H. Jiao, L. Zhao and J. Huang, *Science*, 2021, **373**, 902–907.
42 S. Chen, X. Xiao, B. Chen, L. L. Kelly, J. Zhao, Y. Lin, M. F. Toney and J. Huang, *Sci. Adv.*, 2021, **7**, eabb2412.
43 S. Tan, T. Huang, I. Yavuz, R. Wang, M. H. Weber, Y. Zhao, M. Abdelsamie, M. E. Liao, H.-C. Wang, K. Huynh, K.-H. Wei, J. Xue, F. Babbe, M. S. Goorsky, J.-W. Lee, C. M. Sutter-Fella and Y. Yang, *J. Am. Chem. Soc.*, 2021, **143**, 6781–6786.
44 P.-Y. Lin, A. Loganathan, I. Raifuku, M.-H. Li, Y.-Y. Chiu, S.-T. Chang, A. Fakharuddin, C.-F. Lin, T.-F. Guo, L. Schmidt-Mende and P. Chen, *Adv. Energy Mater.*, 2021, **11**, 2100818.
45 H. Dong, Z. Wu, J. Xi, X. Xu, L. Zuo, T. Lei, X. Zhao, L. Zhang, X. Hou and A. K.-Y. Jen, *Adv. Funct. Mater.*, 2018, **28**, 1704836.
46 A. H. Proppe, A. Johnston, S. Teale, A. Mahata, R. Quintero-Bermudez, E. H. Jung, L. Grater, T. Cui, T. Filleter, C.-Y. Kim, S. O. Kelley, F. De Angelis and E. H. Sargent, *Nat. Commun.*, 2021, **12**, 3472.
47 Y. Zhu, C. Li, J. Chen, Y. Zhang, J. Lu, M. Hu, W. Li, F. Huang, Y.-B. Cheng, H. Park and S. Xiao, *Interdiscip. Mater.*, 2024, **3**, 369–379.
48 S. De Wolf, J. Holovsky, S.-J. Moon, P. Löper, B. Niesen, M. Ledinsky, F.-J. Haug, J.-H. Yum and C. Ballif, *J. Phys. Chem. Lett.*, 2014, **5**, 1035–1039.
49 L. Nakka, Y. Cheng, A. G. Aberle and F. Lin, *Adv. Energy Sustainability Res.*, 2022, **3**, 2200045.
50 D. Glowienka and Y. Galagan, *Adv. Mater.*, 2022, **34**, 2105920.
51 O. Almora, K. T. Cho, S. Aghazada, I. Zimmermann, G. J. Matt, C. J. Brabec, M. K. Nazeeruddin and G. Garcia-Belmonte, *Nano Energy*, 2018, **48**, 63–72.
52 F. Gao, Y. Zhao, X. Zhang and J. You, *Adv. Energy Mater.*, 2020, **10**, 1902650.
53 L. Fu, H. Li, L. Wang, R. Yin, B. Li and L. Yin, *Energy Environ. Sci.*, 2020, **13**, 4017–4056.
54 J. J. Yoo, G. Seo, M. R. Chua, T. G. Park, Y. Lu, F. Rotermund, Y.-K. Kim, C. S. Moon, N. J. Jeon, J.-P. Correa-Baena, V. Bulović, S. S. Shin, M. G. Bawendi and J. Seo, *Nature*, 2021, **590**, 587–593.